Science Bulletin xxx (xxxx) xxx

Contents lists available at ScienceDirect

Science Bulletin

journal homepage: www.elsevier.com/locate/scib

Article

Possible obliquity-forced warmth in southern Asia during the last glacial stage

Cheng Zhao [a,b,c,*], Eelco J. Rohling [d,e], Zhengyu Liu [f], Xiaoqiang Yang [g], Enlou Zhang [a,b], Jun Cheng [h], Zhonghui Liu [i], Zhisheng An [b,j], Xiangdong Yang [a], Xiaoping Feng [a], Xiaoshuang Sun [a], Can Zhang [a], Tianlong Yan [a], Hao Long [a,b], Hong Yan [b,j], Zicheng Yu [k,l], Weiguo Liu [b,j], Shi-Yong Yu [m], Ji Shen [a,c,*]

[a] State Key Laboratory of Lake Science and Environment, Nanjing Institute of Geography and Limnology, Chinese Academy of Sciences, Nanjing 210008, China
[b] Center for Excellence in Quaternary Science and Global Change, Chinese Academy of Sciences, Xi'an 710061, China
[c] School of Geography and Ocean Science, Nanjing University, Nanjing 210023, China
[d] Research School of Earth Sciences, the Australian National University, Canberra ACT 2601, Australia
[e] Ocean and Earth Science, University of Southampton, National Oceanography Centre, Southampton SO14 3ZH, UK
[f] Department of Geography, Ohio State University, Columbus 43210, USA
[g] Department of Earth Sciences, Sun Yat-sen University, Guanghzou 510275, China
[h] Laboratory of Meteorological Disaster, Ministry of Education (KLME)/Joint International Research Laboratory of Climate and Environment Change (ILCEC)/Collaborative Innovation Center on Forecast and Evaluation of Meteorological Disasters (CIC-FEMD), Nanjing University of Information Science and Technology, Nanjing 210044, China
[i] Department of Earth Sciences, University of Hong Kong, Hong Kong, China
[j] State Key Laboratory of Loess and Quaternary Geology, Institute of Earth Environment, Chinese Academy of Sciences, Xi'an 710061, China
[k] Department of Earth and Environmental Sciences, Lehigh University, Bethlehem 18015, USA
[l] Institute for Peat and Mire Research, School of Geographical Sciences, Northeast Normal University, Changchun 130024, China
[m] School of Geography, Geomatics, and Planning, Jiangsu Normal University, Xuzhou 221116, China

ARTICLE INFO

Article history:
Received 29 August 2020
Received in revised form 27 October 2020
Accepted 28 October 2020
Available online xxxx

Keywords:
Southern Asia
Lake sediments
brGDGTs
Annual temperature
The last glacial stage
Obliquity forcing

ABSTRACT

Orbital-scale global climatic changes during the late Quaternary are dominated by high-latitude influenced ~ 100,000-year global ice-age cycles and monsoon influenced ~ 23,000-year low-latitude hydroclimate variations. However, the shortage of highly-resolved land temperature records remains a limiting factor for achieving a comprehensive understanding of long-term low-latitude terrestrial climatic changes. Here, we report paired mean annual air temperature (MAAT) and monsoon intensity proxy records over the past 88,000 years from Lake Tengchongqinghai in southwestern China. While summer monsoon intensity follows the ~ 23,000-year precession beat found also in previous studies, we identify previously unrecognized warm periods at 88,000–71,000 and 45,000–22,000 years ago, with 2–3 °C amplitudes that are close to our recorded full glacial-interglacial range. Using advanced transient climate simulations and comparing with forcing factors, we find that these warm periods in our MAAT record probably depends on local annual mean insolation, which is controlled by Earth's ~ 41,000-year obliquity cycles and is anti-phased to annual mean insolation at high latitudes. The coincidence of our identified warm periods and intervals of high-frequent dated archaeological evidence highlights the importance of temperature on anatomically modern humans in Asia during the last glacial stage.

1. Introduction

Southern Asia, including India monsoon-influenced southwestern China, was a major habitat and dispersal route for anatomically modern *Homo sapiens* following their "out of Africa" migration ~ 100,000 years ago (100 ka) [1,2]. Characterizing climate changes in this monsoon-influenced region, in particularly over the last glacial cycle, may therefore provide important climatic context to this dispersal [2]. So far, long-term monsoon hydroclimate variations in broader Asian monsoon region have been established from a range of different records [3–5], showing strong 23,000-year precession cycles driven by boreal summer insolation [4]. Meanwhile, nearby low-latitude sea-surface temperature (SST) reconstructions display the "classical" ~100,000-year ice-age cycles [6–8], due to the influences of greenhouse-gas (GHG) forcing and showing in-phase with high-latitude climates [6]. Yet, hardly any sufficiently resolved and dated, and

* Corresponding authors.
E-mail addresses: czhao@niglas.ac.cn (C. Zhao), jishen@nju.edu.cn (J. Shen).

https://doi.org/10.1016/j.scib.2020.11.016
2095-9273/

well-quantified land-based annual mean temperature records exist for Indian monsoon-influenced Southern Asia through the last glacial stage and until the present. For example, the most recent syntheses of global temperature over the last deglaciation [9,10] and Holocene [11,12] contain only three summer temperature records in southwestern China. These indicate an overall Holocene summer cooling associated with declining Holocene boreal summer insolation [13,14], with associated reduction in Holocene summer monsoon intensities [3–5]. In contrast to this summer season trend, recent climate simulations indicate that many low-latitude land areas, including Indian-monsoon influenced Southern Asia, experienced an increase in Holocene annual mean temperatures [15]. This contrast between summer and annual mean temperature trends is likely dominated by similarly contrasting changes in Holocene summer and annual mean insolation [13–15], although increasing GHGs could also play a role [16]. According to astronomical calculations, annual mean insolation variations in low latitudes are modulated by obliquity, and therefore (1) are opposite to those at high latitudes, and (2) fluctuate with a fundamentally different periodicity than the precession-dominated variations in summer insolation [17]. Hence, detailed reconstructions of annual mean temperature records in Southern Asia are needed to obtain a comprehensive view of long-term climate changes. This, in turn, may offer valuable climatic context for understanding developments in *Homo sapiens* in Asia (Fig. S1 online) through the last glacial stage.

Branched glycerol dialkyl glycerol tetraethers (brGDGTs) are membrane-spanning lipids produced by heterotrophic bacteria containing two C_{28} alkyl chains with 4–6 methyl substituents and 0–2 cyclopenthy moieties (Fig. S2 online) [18]. The utility in temperature reconstructions is based on the capacity of bacteria to alter the fluidity of their lipid membrane to adjust to colder conditions by producing more methyl branches, and *vice versa* [18]. Because of the consistent variations between lake-surface and air temperatures [19,20] and the relatively weak seasonality in low-latitude areas [21–23], lacustrine brGDGTs-based indices have been proposed as proxies for low-latitude mean annual air temperature (MAAT) reconstructions [23,24]. Meanwhile, long-chain (C_{27}, C_{29}, C_{31}) *n*-alkanes preserved in lake sediment derive mainly from leaf-wax lipids of terrestrial plants [25,26]. Many studies have demonstrated that leaf-wax hydrogen isotope (δD_{wax}, the weighted average δD values of C_{27}-, C_{29}- and C_{31}-alkanes) can be used to record isotopes of rainfall [27–29]. Specifically, in the Indian monsoon region, leaf-wax δD values have been used to record isotopes of Indian monsoon rainfall [27,30–32]. The primary control on rainfall isotopes in the Indian monsoon region is the integrated summer monsoon rainfall between tropical ocean sources and the specific study site through Rayleigh distillation, with lower δD_{wax} values indicating increased rainfall and stronger summer monsoon intensity, and *vice versa* [33,34]. As both δD_{wax} and high-precision U-series dated Chinese speleothem $\delta^{18}O$ records reflect water isotope fractionation processes in the same monsoon rainfall [33,34], and are similarly affected by processes in the hydrological cycle [35], analyzing brGDGTs and leaf wax δD from a single lake sediment core could not only help to constrain the age model of lake sediments beyond the time coverage of the radiocarbon dating method, but also help to identify the potential orbital-scale difference in seasonality between annual temperature and summer monsoon intensity over the last glacial stage.

In addition, paleoclimate models can infer the driving force behind reconstructed climate changes. TraCE 21 ka (TraCE) is the first state-of-art transient simulation of the global climate over the period of the last 21 ka using fully coupled NCAR CCSM3 with T31 spatial resolution (3.75°×3.75°) [36], forced by realistic climatic forcings that comprise orbital insolation [37], atmospheric GHG [38], meltwater discharge/AMOC changes [39], and continental ice sheets (ICE-5G) [40]. Modifications of coastlines and bathymetry are performed at 13.1, 12.9, 7.6 and 6.2 ka for the Barents Sea, the Bering Strait, Hudson Bay, and the Indonesian throughflow, respectively [41,42]. In spite of the limitation of insufficient knowledge about meltwater discharge from continental ice sheets, TRACE 21 ka has been found to reproduce paleoclimatic variations in considerable detail through parallel sensitivity experiments across climate change events [41,42]. Simulations include both the general climate transition from the glacial to interglacial state [10,43], and the main climate change events such as H1, BA, YD during the last deglacial [42,44,45].

In this study, we report both brGDGTs and δD_{wax} records over the past 88,000 years, inferred from exactly the same sample set of a lake sediment core collected in Hengduan Mountains, southwestern China (Fig. S1 online). Together with the advanced TraCE climate simulations, we aim to (1) reconstruct both MAAT and summer monsoon intensity variations since the last glacial stage at a terrestrial site in Indian monsoon-influenced southern Asia; (2) identify the potential orbital-scale seasonal difference between annual temperature and hydroclimate in this region; (3) infer the driving mechanism behind obtained paleoclimate changes; (4) provide a more reliable paleoclimate background for the living conditions of anatomically modern humans.

2. Materials and methods

2.1. Study site

Both Lake Tengchongqinghai (25°07′N, 98°34′E; 1885 m asl) and Lugu Lake (27°41′N, 100°45′E; 2685 m asl) are located in the Hengduan Mountains at the southeastern margin of the Tibetan Plateau (Fig. S1 online), within the influence of the Indian summer monsoon [46]. Lake Tengchongqinghai is close to the Yushuping Archaeology Site, where anatomically modern humans lived at around 30 ka [47] (Fig. S1 online). Lake Tengchongqinghai is a small freshwater crater (maar) lake with a surface area of ~ 0.25 km^2 and a catchment area of ~ 1.5 km^2. The mean water depth is ~ 5.2 m, and the maximum water depth is ~ 8.1 m. The closed lake is mainly recharged by direct precipitation, groundwater, and surface runoff from the catchment basin, with no visible outlet. Lugu Lake is a tectonically formed alpine freshwater lake with a surface area of ~ 50 km^2 and a catchment area of 171.4 km^2. The mean water depth is ~ 40 m, and the maximum water depth is ~ 94 m. The lake resides within an inter-montane basin that is fed mainly by direct precipitation and surface runoff, along with two very small inflowing rivers in the south (Sanjiacun River and Shankua River). The lake is drained via Caohai wetland in the southeast into Gaizu River, a tributary of the Yangtze River [48].

2.2. Sample collection

In 2017, a 2237-cm long sediment core (TCQH17A), reaching the bedrock of the lake bottom, was drilled at ~ 6 m water depth from the center of Lake Tengchongqinghai using a mechanical platform sampling system. After initial descriptions in the laboratory, sediment cores were sliced at 2-cm intervals. In this study, a total of ~ 290 subsamples were selected and analyzed for brGDGTs and leaf-wax hydrogen isotope analyses. In 2010, an 860-cm-long core (LG10) was drilled at ~ 70 m water depth in the center of Lugu Lake using a UWITEC sampling system [48]. After initial descriptions in the laboratory, sediment cores were sliced at 1-cm intervals. In this study, we focus on the top ~ 500 cm for brGDGTs analyses to obtain Holocene MAAT record, with a total of ~ 190 subsamples. We have also collected 20 modern sediment samples from 9 lakes in south-

western China, spanning a large elevational range between ~ 1500 and ~ 4000 m asl and thus a temperature range between ~ 2 and ~ 18 °C (Table S1 online). In addition, 11 and 8 soil samples have been collected from the catchments of Lugu Lake and Lake Tengchongqinghai, respectively.

2.3. Age model

Construction of the chronology for core TCQH17A involves two steps. First, we obtained 13 AMS-^{14}C dates from the top 10 m of the core (going back to 35 ka), mostly from terrestrial plant fragments (Fig. S3 and Table S2 online). The resulting ^{14}C dates were calibrated to calendar ages using IntCal13 calibration curves [49] (Table S2 online) in the program CLAM2.2 [50]. Second, based on the almost identical variations in our δD_{wax} record and the speleothem record [4], we correlated our δD_{wax} record for the section below 10 m with the Chinese speleothem $\delta^{18}O$ records from Hulu, Dongge, and Sanbao Caves, which had been dated previously using the high-precision radiometric U-series dating technique [4], by finding 6 anchor points through graphically correlation of both time series using *Analyseries* [51] (Fig. S3 online). We checked the resulted interval at 88–35 ka with that from the speleothem $\delta^{18}O$ timeseries, using the "cross-correlation" function in the program. That yields a peak correlation (r = 0.7) under their current phase relation of both time series.

The 95% uncertainty of each anchor point is conservatively considered from plus/minus the time span of 2 sampling points of our δD_{wax} analyses. With the top of core TCQH17A setting as −66 year before present (equivalent to the year 2016) because of the well-preserved water–sediment surface, an age model was then developed using linear interpolation method with the CLAM 2.2 code in the software "R". We contend that our age model is robust, based on the observation that both our δD_{wax} and Chinese speleothem $\delta^{18}O$ records show almost identical variations (Fig. S3 online), and the fact that both isotope proxies share the same physical control mechanisms and come from water isotopes in monsoon rainfall.

The age model for core LG10 is transferred from parallel core LG08, which has a chronology based on 13 AMS-^{14}C dates measured on 5 samples of terrestrial plant remains and 8 of bulk organic matter [48]. An old-carbon effect of ^{14}C age 1662 ± 214 a was determined and corrected for regarding bulk organic samples [48]. The resulting 13 ^{14}C dates were calibrated to calendar ages and then an age model was constructed through linear interpolation [48].

2.4. Organic geochemical analysis

Freeze-dried subsamples were ultrasonically agitated in organic solvents (dichloromethane:methanol = 9:1, v/v) for lipid extraction. After saponification of extracted lipids by 6% potassium hydroxide in methanol solution, the neutral lipids were extracted with *n*-hexane, and then separated into apolar (containing *n*-alkanes) and polar fractions (containing GDGTs) with silica gel (100% activated) column chromatography, using *n*-hexane and methanol, respectively [52]. The polar fractions were filtered through a 0.45 μm PTFE polytetrafluoroethylene filter before analysis. The following analyses were performed in the State Key Laboratory of Biogeology and Environmental Geology, China University of Geosciences.

Compound specific hydrogen isotope ratios of *n*-alkanes were measured by a Delta-V advantage Isotope Ratio Mass Spectrometer (IRMS, Thermo Finnigan) connected to a Gas Chromatography (GC) Ultra^{TM} trace (Thermo Finnigan). Apolar fractions containing approximately 300 ng *n*-alkanes were injected into the GC with a splitless mode, with the injector temperature of 290 °C. The GC oven temperature program was 50 °C (held 1 min) to 210 °C at 10 °C/min (held 2 min), then to 300 °C at 6 °C/min, and finally ramped to 310 °C at 10 °C/min (held 25 min). The *n*-alkanes were converted to hydrogen gas using a high-temperature pyrolysis reactor at 1400 °C, and then their hydrogen isotopes were measured by the IRMS. During all the experiments, the H_3^+ factor varied between 3.7 and 4.2 during the sample analysis and daily variation < 0.1 [53]. The stability of the IRMS was checked with an *n*-alkane mixture (*n*-C_{23}, *n*-C_{25}, *n*-C_{27}, *n*-C_{29}, and *n*-C_{31} alkane) and the Indiana A4 mixture with known δ^2H values between every two samples. Squalane (δ^2H value: −167‰) was used as the internal standard. Standard deviation for hydrogen isotope analysis was less than ± 5‰, based on at least duplicate analyses. Results are reported in the delta notation (‰) relative to the Vienna Standard Mean Ocean Water standard (VSMOW). The down-core δD results from C_{27}, C_{29}, and C_{31}–alkanes are shown in Fig. S4 (online).

Identification and quantification of brGDGTs were performed using Agilent 1200 series liquid chromatograph linked to a triple quadrupole mass spectrometer (LC-MS2) system, equipped with auto-injection mode and Masshunter qualitative software. The polar fractions were spiked with an aliquot of internal C_{46} standard and re-dissolved in 300 μL solvents (*n*-hexane:ethyl acetate, EtOA, 84:16, v/v) with injection volume of 10 μL. Separation of 5- and 6-methyl brGDGTs isomers was achieved with two Silica columns in tandem (each 150 mm × 2.1 mm, 1.9 μm, Thermo Finnigan; USA), maintained at 40 °C. The elution gradients of GDGTs were *n*-hexane:EtOA solvent (84:16, v/v) for the first 5 min, followed by a linear gradient change to *n*-hexane:EtOA solvent (82:18, v/v) from 5 to 65 min and then to 100% EtOA for 21 min, followed by 100% EtOA for 4 min to wash the column and then back to *n*-hexane:EtOA solvent (84:16, v/v) to equilibrate the column. The constant flow rate was 0.2 mL/min throughout. The MS conditions were: nebulizer pressure 60 psi, vaporizer temperature 400 °C, drying gas flow rate 6 L/min and temperature 200 °C, capillary voltage 3500 V, corona 5 μA. Selected ion monitoring (SIM) was used, monitoring at m/z 1050, 1048, 1046, 1036, 1034, 1032, 1022, 1020, 1018 for the regular of brGDGTs. Quantification of GDGTs was achieved by using an external standard and integrating peaks areas of the $[M + H]^+$ ions, assuming an identical response factor for GDGTs. The 5- and 6-methyl brGDGTs were assigned as described in Ref. [54].

2.5. brGDGT data analyses, MAAT reconstruction and uncertainty assessment

We calculate fractional abundances of summed tetra-, penta- and hexa-methylated brGDGTs of the 20 modern samples from the 9 lakes in southwestern China, down-core samples from both core LG10 and core TCQH17A, and modern soil samples from both lake catchments. We also compare with results of modern samples from East African lakes [24] and global soils [55] (Fig. S5 online). All these results derive from the new brGDGT analytical method, with separation of 5-methyl and 6-methyl isomers.

We choose recently proposed Index1 [55] as the proxy for mean annual air temperature (MAAT) reconstructions, which is also one of the recommended calibrations for East African lakes [24]. To fully propagate the uncertainties of the calibration and our temperature reconstructions, we performed a linear ordinary least-squares regression of Index1 against MAAT, yielding a calibration line and its 2σ confidence interval (Fig. S6a online). The predictive ability of our model and the uncertainty in our reconstruction were evaluated by bootstrapping, which generated 5000 replicates assumed to mimic the actual distribution of the model parameters (Fig. S6b, c online). The bootstrapped coefficient of determination (R^2) and root mean squared error of prediction (RMSEP) are 0.91 and 2.49, respectively. Uncertainties of MAAT time-series were

calculated from the bootstrapping and expressed in terms of 95% confidence interval.

3. Results and discussion

3.1. Evaluation and validation of MAAT reconstruction

The results from both modern and down-core lake sediments in southwestern China are consistent with those from East African Lakes (Fig. S5a, c online). Results from soils in both lake catchments are also consistent with those from global soils (Fig. S5b, d online). This suggests that brGDGT distributions in southwestern China follow closely the global or broader-scale lacustrine/soil brGDGT patterns with separation of 5-methyl and 6-methyl isomers (Fig. S5 online).

However, brGDGT distributions between soils and lake sediments (both down-core and modern samples) are distinct in either Lugu or Tengchongqinghai catchments. At Lugu Lake, for example, fractional abundances of hexa- (0.3–0.46) and tetra-methylated (0.11–0.18) brGDGTs in lake sediments have ranges that are distinct from those in catchment soils (0.02–0.2 for hexa- and 0.19–0.62 for tetra-) (Fig. S5a, b online). While at Lake Tengchongqinghai, fractional abundances of penta- (0.3–0.5) and tetra-methylated (0.3–0.6) brGDGTs in lake sediments also have ranges that are distinct from those in catchment soils (0–0.3 for penta- and 0.7–0.9 for tetra-) (Fig. S5c, d online). Although we cannot completely exclude any brGDGT contribution from soils based only on these differences, our comparison still suggests that brGDGT sources in both lakes are dominated by autogenic lacustrine origins rather than soil contributions in both modern and downcore sediments.

Considering the broadly similar environmental variables and climatic background of both lake groups (Table S1 online), and the similar brGDGT-MAAT calibration functions based on East African lakes (MAAT = 12.22 + 18.79 × Index1, R^2 = 0.92) and SW Chinese lakes (MAAT = 11.08 + 20.69 × Index1, R^2 = 0.84), it is reasonable to combine the results from both lake groups to obtain a more reliable function (MAAT = 12.18 + 19.11 × Index1, R^2 = 0.92, RMSE = 2.49 °C) for our study area (Fig. S6a online). Also, study of brGDGTs in African lakes has demonstrated that MAAT explains the majority of the variations in the East African lake brGDGT data (by comparing with other variables such as lake depth, surface and bottom pH, conductivity, surface area, surface and bottom dissolved oxygen, etc.), and that the inferred MAAT calibrations may be appropriate in tropical lakes outside East Africa [24]. With all our downcore brGDGTs falling within range of these modern lake sediments, the calibration is robust for reconstructing low-latitude MAAT changes for this study.

We compare the Index1-based and traditional MBT'$_{5ME}$-based MAAT reconstructions (Fig. S7 online), and find the Index1-based calibration can get a more realistic MAAT at Lake Tengchongqinghai which is comparable to instrumental data, although both time series vary consistently. For instance, the reconstructed core-top temperature of ~ 17.9 °C agrees well (within its 2-sigma uncertainties) with the modern mean annual temperature of 17.5 °C at the year 2016 obtained from the nearby Baoshan Meteorological Station. We further validate the Holocene MAAT of Lake Tengchongqinghai with another reconstruction from the nearby higher-elevation, larger Lugu Lake, using exactly the same method based on the Index1. Both records show a similar overall trend in the Holocene, but the Lugu record shows less high-frequency variability and more similarity to the TraCE model output (Figs. S7 and S8 online). In addition, another brGDGT-inferred MAAT record from Lake Tengchongqinghai [56], re-calculated by our new calibration function, shows an overall similar pattern with ours during the past 50 ka (Fig. S7a online).

In addition, we calculate the Branched Isoprenoid Tetraether index (BIT) and CBT'-derived pH records for both lakes, although the recent study shows that brGDGT-derived lake pH values have larger uncertainties [24]. In core TCQH17A from Lake Tengchongqinghai, BIT values fall in a quite small range (0.97 to 1) relative to many other lakes (Fig. S7 online), which indicates a rather stable microbial populations over the past ~ 88 ka. At orbital scales, there are small changes (up to 0.03) in BIT values which show some similarities with variations of our δD_{wax}-derived monsoon intensities (Fig. S7 online), indicating that orbital-scale BIT changes have been probably driven by monsoon rainfall rather than MAAT. Similarly, orbital-scale changes in inferred pH values also show similarities with changes in our monsoon intensity record (Fig. S7 online). In addition, lithology of the core, although without distinct lithofacies variations, still shows subtle changes consistent with orbital-scale monsoon variations (Fig. S3 online). These findings suggest that our inferred MAAT changes are independent from other environmental variables at Lake Tengchongqinghai.

At Lugu Lake, the inferred downcore pH values do not show a clear correlation with our reconstructed MAAT data either (Fig. S8 online). Calculated downcore BIT values are relatively stable at ~ 0.9 before 10 ka and then decreased to ~ 0.6 during over the past 10 ka (Fig. S8 online). Although BIT values in the Holocene section are roughly anti-phased with our MAAT data, they do not show an obvious change during the last deglaciation when the MAAT experienced a temperature drop at 13–12 ka (the Younger Dryas event) and then a warming trend at 12–10 ka. Similar to Lake Tengchongqinghai, therefore, brGDGT-inferred MAAT in Lugu Lake does not seem to be substantially influenced by other environmental variables, as was also indicated in modern East African lakes [24]. In addition, the MAAT record at Lugu Lake shows a consistent change with that from TraCE simulations, further supporting the reliability of this MAAT record (Figs. S7 and S8 online).

3.2. Reconstructed MAAT variations in southwestern China

Our MAAT record from Lake Tengchongqinghai shows pronounced orbital-scale periodic warm intervals since the last glaciation, including an ~ 2.5 °C warming interval from 88 to 71 ka, an up to ~ 2 °C warmer period from 45 to 22 ka, and a progressive ~ 3 °C warming from the end of the last glacial maximum around 19 ka to the late Holocene (Fig. 1c). During the intercalated colder intervals, MAAT values averaged about 14–15 °C (Fig. 1c). The inferred temperature difference of ~ 3 °C between means for the last glacial maximum and Holocene agrees with previous estimates of 2–4 °C for low-latitude oceans [57] and many low-elevation sites in tropical terrestrial regions [58,59].

The pattern of temporal variability in our reconstructed MAAT record differs markedly from that of Asian summer monsoon intensity records, including our own δD_{wax} record from the same sample set and the absolute-dated Chinese speleothem $\delta^{18}O$ records [4] (Fig. 1a – c). In particular, our MAAT data do not show the ~ 23,000-year precession cycle, which is especially prominent in the summer monsoon-intensity records from Chinese caves (Fig. 1a – c). The cave records are strongly affected by hydroclimate variations throughout low-latitude summer monsoon areas [4], which is corroborated by the agreement with our δD_{wax} record. Summer monsoons were intense during Marine Isotope Stage 5a (MIS5a) and weak during MIS 4. Conversely, our MAAT reconstruction shows that the warm period lagged peak summer monsoon intensities in MIS 5a as recorded by δD_{wax} from the same set sample. Moreover, the warm period extended from MIS 5a into early MIS 4 (Fig. 1a – c). During MIS 3, summer monsoon intensities were relatively high, but MAAT was low throughout the first half

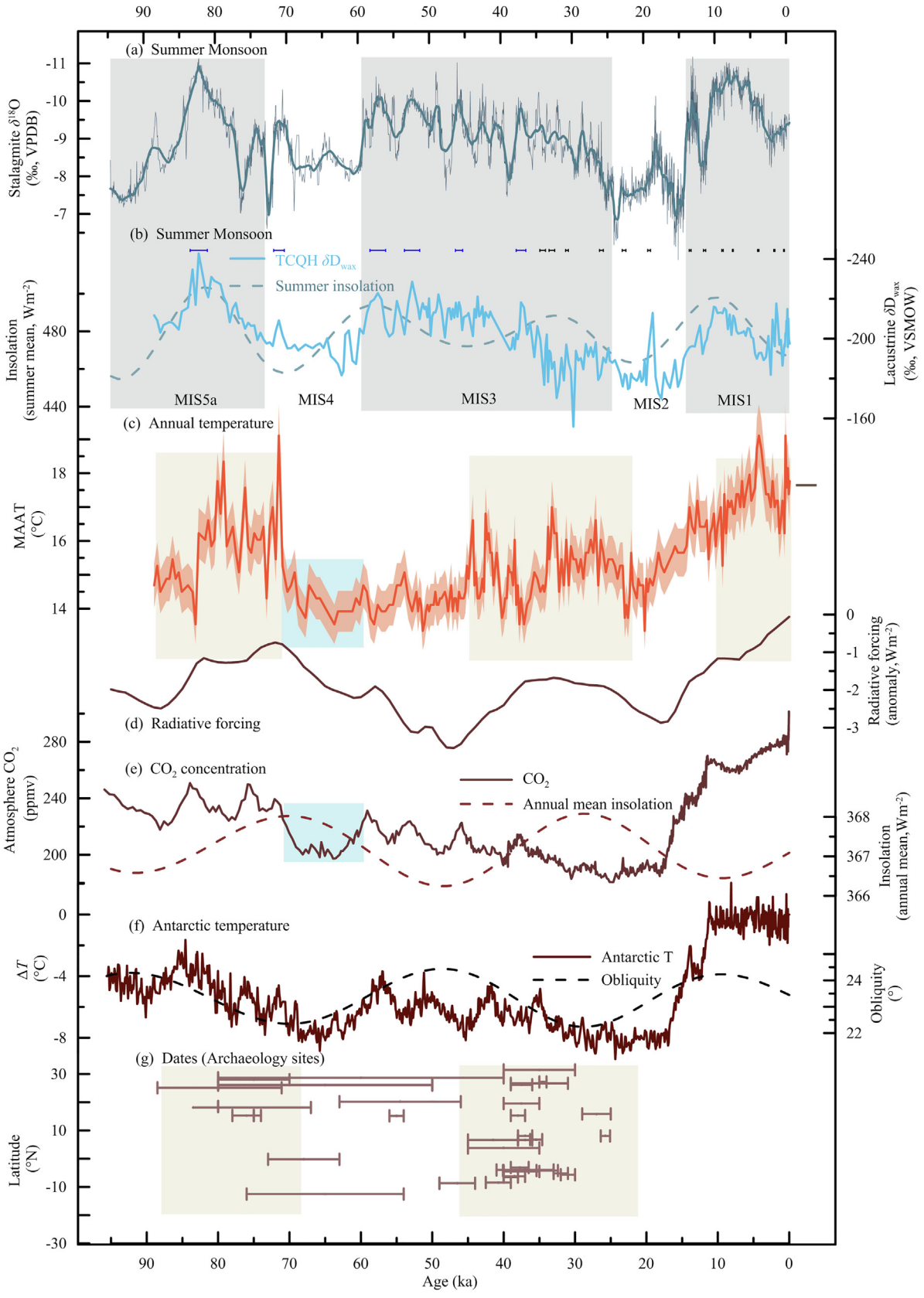
(a) Summer Monsoon
Stalagmite δ18O (‰, VPDB)
-11
-10
-9
-8
-7
(b) Summer Monsoon
TCQH δDwax
Summer insolation
Insolation (summer mean, Wm-2)
480
440
Lacustrine δDwax (‰, VSMOW)
-240
-200
-160
MIS5a
MIS4
MIS3
MIS2
MIS1
(c) Annual temperature
MAAT (°C)
18
16
14
(d) Radiative forcing
Radiative forcing (anomaly, Wm-2)
0
-1
-2
-3
(e) CO2 concentration
CO2
Annual mean insolation
Atmosphere CO2 (ppmv)
280
240
200
Insolation (annual mean, Wm-2)
368
367
366
(f) Antarctic temperature
Antarctic T
Obliquity
ΔT (°C)
0
-4
-8
Obliquity (°)
24
22
(g) Dates (Archaeology sites)
Latitude (°N)
30
10
-10
-30
90
80
70
60
50
40
30
20
10
0
Age (ka)

Fig. 1. Comparison of the reconstructed annual temperature at Lake Tengchongqinghai and other regional and global paleoclimate reconstructions. (a) Speleothem $\delta^{18}O$ data and its 50-point moving averages (thick dark cyan) from Dongge-Hulu-Sanbao Caves in China [4]. VPDB, Vienna Pee Dee belemnite. (b) Lake Tengchongqinghai δD_{wax} record (this study) and summer mean isolation (June-July-August) at 30°N [17]. VSMOW, Vienna Standard Mean Ocean Water. Ticks on top of this panel represents radiocarbon dates (black) and anchor points (blue) between Chinese speleothem $\delta^{18}O$ and Lake Tengchongqinghai δD_{wax} with 2σ errors. (c) Lake Tengchongqinghai MAAT record (this study, shaded envelope representing its 2σ uncertainty). The brown tick on the right indicates modern instrumental annual temperature. (d) Calculated radiative forcing anomaly based on GHG (including both CO_2 and CH_4, after Ref. [84]) and annual mean isolation at 30°N, both forcings are normalized to their own pre-industrial value. (e) Atmospheric CO_2 concentrations from the EPICA Dome C [60], and annual mean isolation at 30°N [17]. (f) Reconstructed temperature anomalies inferred from $\delta^{18}O$ values of Vostok ice core in the Antarctic [61] and Earth's obliquity [17]. (g) Dating results of archaeology sites of modern humans in low-latitude Asia [1] with 2σ errors, together with two new results from southwestern China and the Tibetan Plateau (Methods and Fig. S1 online). Marine isotope stages are indicated by gray shaded areas, obliquity-forced warm periods are indicated by grayish-yellow shaded areas. The low-CO_2-concentration interval related with the cold period between 71 and 60 ka is highlighted by the light-blue shaded area.

of this interval (Fig. 1a – c). Summer monsoon intensities were low during MIS 2, while a warm period revealed by our MAAT data spanned the later stage of MIS 3 and early MIS 2 until 22 ka (Fig. 1a – c). During the Holocene, summer monsoon intensity decreased, whereas MAAT continued to increase since the last glacial maximum (Fig. 1a – c).

Our MAAT record also differs substantially from global-scale and many regional temperature reconstructions obtained from marine sediments, polar ice cores, and Chinese loess sections. Atmospheric CO_2 concentrations [60] (Fig. 1e), high-latitude temperatures from Antarctic [61] (Fig. 1f) and Greenland ice cores [62], and global mean SST [63] all display an overall declining trend during the last glacial stage, typical of the so-called "saw-tooth"-shaped ~ 100,000-year global glacial-interglacial cycle. Summer-biased temperature records derived from soil brGDGTs from the mid-latitude Chinese Loess Plateau, where the brGDGT producer organisms are sensitive to moisture availability in this semi-arid region and probably experience optimum growth during East Asian summer monsoon season [64,65], also show this glacial-interglacial pattern [64–66], although some display strong ~23,000-year precessional cycles similar to those characteristics of summer monsoon intensities [65]. In contrast, our Lake Tengchongqinghai MAAT shows two long warm intervals in the cold last glacial stage, which reach amplitudes close to the full glacial-interglacial range (Fig. 1c). Conversely polar and global temperatures, and atmospheric CO_2 levels, were relatively high in the period centered on 55 ka (Fig. 1e, f), while our Tengchongqinghai MAAT stayed low (Fig. 1c).

A classic "saw-tooth"-shaped global glacial-interglacial cycle has also been reported for many low-latitude SST reconstructions [6–8]. However, some more proximal low-latitude SST records from the western Arabian Sea [67], Bay of Bengal [68], and northern Arabian Sea [69] seem more consistent with our MAAT record (Fig. S9 online). We infer that the driver of annual mean temperature variations in southwestern China, and - at least - in the aforementioned northern sectors of the Indian Ocean, was fundamentally different from the driver of summer monsoon intensity and that of the global temperature, which is strongly influenced by northern high-latitude climate.

During the Holocene, our MAAT data show an overall warming trend, which contrasts with the cooling trend in stacked records of global annual temperature [11,12]. Within low latitudes, most available Holocene temperature records, including SSTs and terrestrial temperatures, derive from locations outside of the Indian monsoon-influenced southern Asia [11]. These data usually show contrasting annual temperature trends at different areas, including both warming and cooling in the Indo-Pacific Warm Pool [70,71], the Indian Ocean [72,73], and tropical Africa [74]. This indicates the existence of major spatial heterogeneity in low-latitude Holocene annual temperature trend. Within Indian-monsoon influenced terrestrial regions, available Holocene temperature records concern summer temperatures in southwestern China [13,14], which show a cooling trend through the Holocene that contrasts with the warming trend in our MAAT record (Fig. 2). This difference between summer-specific and annual mean temperatures in southwestern China highlights the critical importance of understanding seasonality in Indian-monsoon influenced terrestrial temperature reconstructions. In the following, we disentangle the different drivers on our MAAT record using TraCE simulations [45].

3.3. Driving force of Holocene temperature changes in southern Asia

The two MAAT records from Lake Tengchongqinghai and Lugu Lake show similar overall trends and amplitudes of change (Fig. 2a, b), indicating our data can capture regional temperature pattern in southwestern China. Then, we compare both MAAT records with the TraCE simulations [45]. Model-simulated MAAT records under all forcings for the study region show strong similarity with our two MAAT reconstructions, with respect to both the general trend and the amplitudes of overall changes (Fig. 2a, b). A bit discrepancy likely exists over the late Holocene. Our MAAT records also show a temperature decrease at that time (Fig. 2a), which agrees with a recent temperature reconstruction for North America and Europe [75], but which is not apparent in TraCE simulations (Fig. 2a, b). We suggest that this may reflect a lack of influences of volcanic and solar-variability [76], as well as anthropogenic forcing in the TraCE simulations, which certainly needs to be tested with additional paleoclimate data and models in the future.

Regarding the overall trend of annual mean temperatures, TraCE simulations with individual forcings reveal that the deglacial warming in our record is mainly forced by GHG increase, while Holocene warming is mainly forced by increasing low-latitude annual mean insolation with an additional GHG contribution after 6 ka, with very limited influences of ice-sheet and melt-water changes (Fig. S10 online). Although a general Holocene warming in low latitudes are evident in TraCE and other simulations [15], an obvious spatial heterogeneity also exists (Fig. 3). In these models, the warming Holocene pattern with strong sensitivity to annual insolation is coherent throughout tropical northern Africa (~10°–20°N), the southern Arabia Peninsula, India, and southwestern China, which cover our study site (Fig. 3b) (see also Ref. [15]). Beyond these regions, the influence of annual mean insolation is relatively weak (Fig. 3b) (see also Ref. [15]), and this is unfortunately where most available low-latitude records derive from Ref. [11]. Notably, some local factors could override the effect of annual insolation, and induce substantial spatial heterogeneity in Holocene annual temperature trends. For instance, Holocene SST discrepancies in the Indo-Pacific Warm Pool and Indian Ocean may be attributed to monsoon-induced ocean circulation patterns [71,72], influences of northern high-latitude climates [70] and/or seasonal bias in SST proxies [73,77], while Holocene temperature changes in tropical and southern Africa have been linked to a complex interplay of local annual maximum insolation [78], tropical hydrology [79], southwestern Indian Ocean SST [80], and northern high-latitude climates [81,82]. Fortunately, model simulations suggest that our study site is in the less-complicated region where local annual insolation influences are dominant (Fig. 3b) (see also

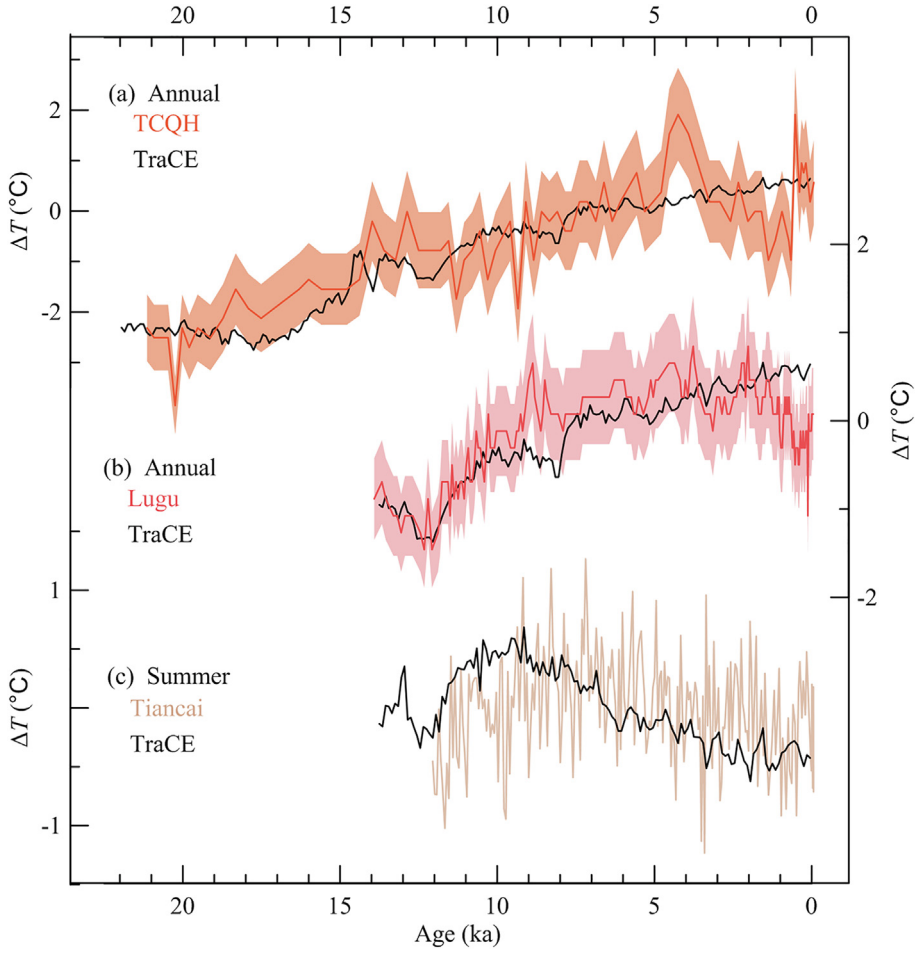

Fig. 2. Comparison of reconstructions and TraCE outputs for annual and summer temperatures in southwestern China. (a) Lake Tengchongqinghai MAAT reconstructions with 2σ uncertainty (this study) and TraCE output of Holocene annual mean temperature. (b) Lugu Lake MAAT reconstructions with 2σ uncertainty (this study) and TraCE output of Holocene annual mean temperature. (c) Tiancai Lake (southwestern China) July temperature reconstructions by chironomids [14] and TraCE output of Holocene summer temperature. All records and TraCE outputs are normalized to their own Holocene mean. TraCE outputs are for our study region in southwestern China, and under full forcing. Results from individual forcing can be found in Fig. S10 (online).

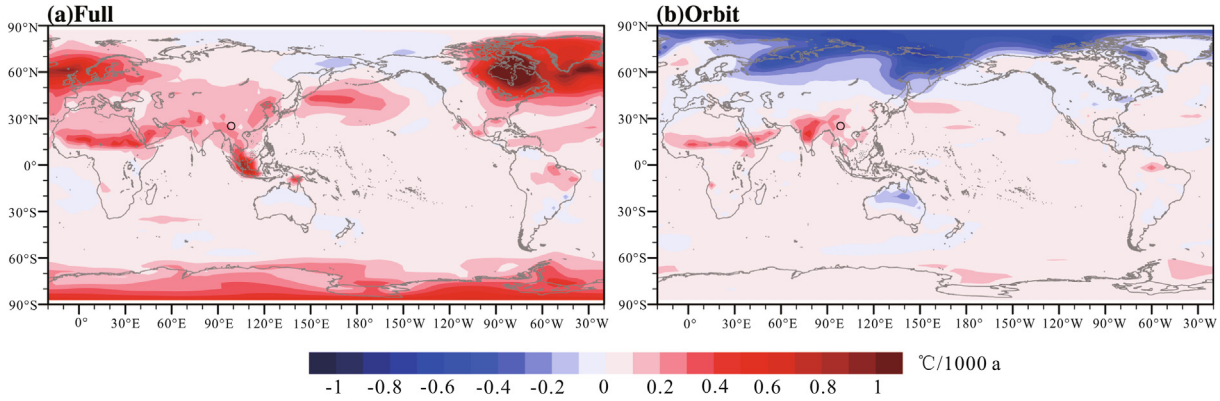

Fig. 3. Evaluation of spatial influence of annual-insolation during the Holocene in TraCE. (a) Holocene annual temperature tendency (from 10 to 1 ka) under full forcing, which shows that most areas are warming. (b) Holocene annual temperature tendency under single orbital forcing, which shows that low latitude areas, including southwestern China, India, Tropical Africa, southern Arabian Peninsula, and eastern Amazonia, are most sensitive to local-annual-insolation forced warming. The black circle in southwestern China indicates our study site.

Ref. [15]). Regarding summer temperatures, both reconstructions (Fig. 2c) and TraCE output (Fig. S10 online) indicate an overall decreasing trend through the Holocene for southwestern China, which is strongly related to local (boreal) summer insolation (Figs. 2c and S10 online). This summer temperature trend contrasts markedly with our observed and simulated warming trend through the Holocene in annual mean temperatures, which relate to annual mean insolation (Figs. 2a, b and S10 online).

While we find good agreement between the TraCE simulation records and our observed annual mean temperature reconstruc-

tions for southwestern China, TraCE (and other models) also suggest a global mean Holocene warming trend, driven by declining high-latitude ice sheets and slightly increasing atmospheric CO_2 concentrations [16]. This contrasts with global-mean proxy-based paleotemperature syntheses, which suggest a global-mean annual-mean cooling through the Holocene [11,12]. This discrepancy has been attributed to the summer bias in many paleotemperature records [16,75,83], and especially in those from northern mid- and high-latitude regions where most records in the global compilations come from [11,12,15]. In addition, a recent synthesis of model simulations infers that this discrepancy can be related to Arctic amplification and sea ice loss driven by boreal summer insolation, which would cause decreasing Holocene annual mean temperatures in the northern extratropics [15], which are overrepresented in the global-mean proxy-based paleotemperature syntheses. However, all these models consistently show a warming Holocene trend in our study region, with a considerable contribution of local annual mean insolation [15,16]. This is consistent with our new record.

3.4. Possible obliquity-induced warmth in southern Asia during the last glacial stage

Although the TraCE simulation does not extend beyond 21 ka, the identified annual mean insolation and atmospheric GHG (mainly CO_2) concentrations may also work for Lake Tengchongqinghai record at longer timescales. Indeed, the orbital-scale variations in our MAAT record coincide with the timing of changes in both factors within the last glacial stage. From 88 to 71 ka, for instance, the observed ~ 2.5 °C warming in MAAT coincided with rising annual mean insolation along with 20–30 ppm elevated atmospheric CO_2 concentrations from a background value of ~ 220 ppm. The abrupt ending of this warm period coincides with a sharp CO_2 decline of ~ 40 ppm, along with decreasing annual mean insolation. From 45 to 22 ka, increased annual mean insolation in the region of Lake Tengchongqinghai alone, without CO_2 increase, sufficed to increase annual mean temperature by about ~ 2 °C. During the last deglaciation, ~ 3 °C warming occurred in response to a rapid CO_2 increase of ~ 80 ppm, despite an overall decline of annual mean insolation.

In order to better evaluate the influence of local annual insolation and GHG on our MAAT record, we make a simple estimation by combing these two radiative forcings after measuring both of them in W/m^2 (conversion of GHG forcing after Ref. [84], which include both CO_2 and CH_4), albeit they have different wavelengths (Fig. 1d). The calculated result suggests this combined radiative forcing is basically consistent with our MAAT record during the past ~ 90 ka (Fig. 1d). The three peaks at 88–71, 45–22 and 14–0 ka correspond well with the three warm periods in our MAAT record (Fig. 1d). However, the combined forcing decreased gradually at 71–60 ka and reached its lowest value around 45 ka, while our MAAT reached its lowest value at the entire 71–45 ka interval (Fig. 1d). This mismatch may be largely due to the simplicity of the estimation method for radiative forcings, which does not take into account many additional processes such as atmospheric-oceanic circulations and land covers, which could amplify these radiative forcings and induce large changes. Also, the calculated insolation is at the top of the atmosphere rather than the Earth surface, which likely overestimates the forcing at the land surface. In addition, other trace gases such as N_2O will increase the GHG radiative forcing as well. Together with these uncertainties, we speculate those additional processes could be spatial- and time-variable, which certainly needs to be further studied with a data and model synthesis in the future.

It is probably that the identified warm periods at 88–71 and 45–22 ka in our MAAT record were mainly induced by local annual mean insolation. The rise and fall of low-latitude annual mean insolation is strongly regulated by the ~ 41,000-year cycle of obliquity or tilt of Earth's axis relative to its orbital plane (Fig. 1f), which exerts opposite annual mean insolation effects in high and low latitudes, with the switch-over centered on 40°–45° latitude [17,84]. Decreased obliquity reduces annual mean insolation in high-latitude regions, but increases annual mean insolation in low-latitude regions [17,84]; this was the case during the warm intervals at 88–71 and 45–22 ka recorded in our MAAT record. Compared with the relatively small amplitudes of this effect during the Holocene, the much larger increase in low-latitude annual mean insolation during the 88–71 and 45–22 ka intervals could override the influence of northern high-latitude climate and other possible localized factors, and may cause warmer conditions over some larger areas, such as the northern reaches of the Indian Ocean (Fig. S9 online). Our compilation and new data may reveal pervasive and widespread impacts of obliquity-induced annual mean insolation changes in the low latitudes, particularly in Southern Asia. This influence is recognized even in the Holocene, when obliquity impacts were relatively small (Fig. 1f). However, we notice many other paleoclimate records, although from the simulated annual-insolation sensitive regions such as low-latitude Africa, show some contrasting temperature changes [74] and inconsistent with our record [74,85]. Therefore, our finding and model simulations need to be assessed with additional temperature records from low-latitude land and ocean sites with excellent chronology, high sampling resolutions, and preferably with clear distinction of seasonal signals.

4. Conclusions and implications

We present the first, highly-resolved record of annual mean temperature in Indian-monsoon influenced Southern Asia that covers the entire last glacial cycle. It demonstrates that orbital-scale changes in annual mean temperature were decoupled from summer monsoon fluctuations in the region. In particular, we recognize two key intervals (88–71 and 45–22 ka) of elevated annual mean temperature that are close to the full glacial-interglacial range. With the output of TraCE simulations and comparing with forcing factors, we find these warm periods are probably forced by local annual mean insolation and secondarily GHGs, while the monsoon intensity tends to be closely associated with season-specific summer insolation.

Our findings may offer new insight into the living conditions of anatomically modern humans in Asia, providing our observed annual-insolation-induced MAAT changes also works in broader areas as suggested by TraCE and other models [15]. The two warm intervals within the last glacial stage coincide with intervals of highest frequencies of dated evidence [1] for anatomically modern humans in Asia (Fig. 1c, g). While monsoon records (Fig. 1a, b) also show generally high summer monsoon intensities in these warm intervals, the interval 61–45 ka has high monsoon intensities but low frequencies of dated archaeological evidence. This suggests that the grouping of archaeological datings is more consistent with the occurrence of our warm intervals (or warmth plus active monsoons), rather than with active monsoons alone. Thus, our new temperature record may highlight the importance of temperature for anatomically modern humans in these regions within the last glacial stage.

Conflict of interest

The authors declare that they have no conflict of interest.

Acknowledgments

This work was supported by the Strategic Priority Research Program of Chinese Academy of Sciences (XDB40010200 and XDA2009000004), the Program of Global Change and Mitigation, Ministry of Science and Technology of China (2016YFA0600502), and the National Natural Science Foundation of China (41877293, 41672162, 41977381 and 41472315). We thank the editors and three anonymous referees for their thoughtful reviews and constructive suggestions. We thank Le Yang from Nanjing Institute of Geography and Limnology, Chinese Academy of Sciences for organic geochemical pretreatments, Xianyu Huang and Huan Yang from China University of Geosciences (Wuhan), Jingjing Li from Nanjing Institute of Geography and Limnology, Chinese Academy of Sciences, and Shaopeng Gao from Institute of Tibetan Plateau Research, Chinese Academy of Sciences for brGDGTs analyses and hydrogen isotope analyses. We thank Jack Williams from University of Wisconsin-Madison (USA), Haibin Wu from Institute of Geology and Geophysics, Chinese Academy of Sciences, Huayu Lu from Nanjing University (China) for helpful discussions. Maps in this article were reviewed by Ministry of Natural Resources of the People's Republic of China(GS(2020)6246)).

Author contributions

Cheng Zhao and Ji Shen designed the study. Cheng Zhao, Xiaoqiang Yang, Enlou Zhang collected sediment cores. Zhengyu Liu and Jun Cheng performed climate simulations and analyses. Xiaoping Feng, Xiaoshuang Sun, Can Zhang, and Tianlong Yan performed lab work and data analyses. Shi-Yong Yu performed statistical analyses. Cheng Zhao and Eelco J. Rohling led writing the paper. All authors contributed to discussion the results and writing of the manuscript.

Appendix A. Supplementary materials

Supplementary materials to this article can be found online at https://doi.org/10.1016/j.scib.2020.11.016.

References

[1] Bae CJ, Douka K, Petraglia MD. On the origin of modern humans: Asian perspectives. Science 2017;358:eaai9067.
[2] Timmermann A, Friedrich T. Late Pleistocene climate drivers of early human migration. Nature 2016;538:92–5.
[3] Beck JW, Zhou W, Li C, et al. A 550,000-year record of East Asian monsoon rainfall from ^{10}Be in loess. Science 2018;360:877–81.
[4] Cheng H, Edwards RL, Sinha A, et al. The Asian monsoon over the past 640,000 years and ice age terminations. Nature 2016;534:640–6.
[5] An ZS, Clemens SC, Shen J, et al. Glacial-interglacial Indian summer monsoon dynamics. Science 2011;333:719–23.
[6] Herbert TD, Peterson LC, Lawrence KT, et al. Tropical ocean temperatures over the past 3.5 million years. Science 2010;328:1530–4.
[7] Oppo DW, Sun Y. Amplitude and timing of sea-surface temperature change in the northern South China Sea: dynamic link to the East Asian monsoon. Geology 2005;33:785.
[8] Saraswat R, Nigam R, Weldeab S, et al. A first look at past sea surface temperatures in the equatorial Indian Ocean from Mg/Ca in foraminifera. Geophys Res Lett 2005;32:L24605.
[9] Shakun JD, Clark PU, He F, et al. Global warming preceded by increasing carbon dioxide concentrations during the last deglaciation. Nature 2012;484:49–54.
[10] Clark PU, Shakun JD, Baker PA, et al. Global climate evolution during the last deglaciation. Proc Natl Acad Sci USA 2012;109:E1134–42.
[11] Kaufmann D, McKay N, Routson C, et al. A global database of Holocene paleotemperature records. Sci Data 2020;7:115.
[12] Marcott SA, Shakun JD, Clark PU, et al. A reconstruction of regional and global temperature for the past 11,300 years. Science 2013;339:1198–201.
[13] Wu D, Chen X, Lv F, et al. Decoupled early Holocene summer temperature and monsoon precipitation in southwest China. Quat Sci Rev 2018;193:54–67.
[14] Zhang E, Chang J, Cao Y, et al. Holocene high-resolution quantitative summer temperature reconstruction based on subfossil chironomids from the southeast margin of the Qinghai-Tibetan Plateau. Quat Sci Rev 2017;165:1–12.
[15] Park H-S, Kim S-J, Stewart AL, et al. Mid-Holocene Northern Hemisphere warming driven by Arctic amplification. Sci Adv 2019;5:eaax8203.
[16] Liu Z, Zhu J, Rosenthal Y, et al. The Holocene temperature conundrum. Proc Natl Acad Sci USA 2014;111:E3501–5.
[17] Laskar J, Robutel P, Joutel F, et al. A long term numerical solution for the insolation quantities of the Earth. Astron Astrophys 2004;428:261–85.
[18] Weijers JWH, Schouten S, van den Donker JC, et al. Environmental controls on bacterial tetraether membrane lipid distribution in soils. Geochim Cosmochim Acta 2007;71:703–13.
[19] Loomis SE, Russell JM, Heureux AM, et al. Seasonal variability of branched glycerol dialkyl glycerol tetraethers (brGDGTs) in a temperate lake system. Geochim Cosmochim Acta 2014;144:173–87.
[20] Livingstone DM, Lotter AF. The relationship between air and water temperatures in lakes of the Swiss Plateau: a case study with palæolimnological implications. J Paleolimnol 1998;19:181–98.
[21] Shanahan TM, Hughen KA, Van Mooy BAS. Temperature sensitivity of branched and isoprenoid GDGTs in Arctic lakes. Org Geochem 2013;64:119–28.
[22] Loomis SE, Russell JM, Ladd B, et al. Calibration and application of the branched GDGT temperature proxy on East African lake sediments. Earth Planet Sci Lett 2012;357-358:277–88.
[23] Tierney JE, Russell JM, Eggermont H, et al. Environmental controls on branched tetraether lipid distributions in tropical East African lake sediments. Geochim Cosmochim Acta 2010;74:4902–18.
[24] Russell JM, Hopmans EC, Loomis SE, et al. Distributions of 5- and 6-methyl branched glycerol dialkyl glycerol tetraethers (brGDGTs) in East African lake sediment: effects of temperature, pH, and new lacustrine paleotemperature calibrations. Org Geochem 2018;117:56–69.
[25] Cranwell PA, Eglinton G, Robinson N. Lipids of aquatic organisms as potential contributors to lacustrine sediments—II. Org Geochem 1987;11:513–27.
[26] Eglinton G, Hamilton RJ. Leaf epicuticular waxes. Science 1967;156:1322–35.
[27] Contreras-Rosales LA, Jennerjahn T, Tharammal T, et al. Evolution of the Indian Summer Monsoon and terrestrial vegetation in the Bengal region during the past 18 ka. Quat Sci Rev 2014;102:133–48.
[28] Tipple BJ, Pagani M. Environmental control on eastern broadleaf forest species' leaf wax distributions and D/H ratios. Geochim Cosmochim Acta 2013;111:64–77.
[29] Sachse D, Billault I, Bowen GJ, et al. Molecular paleohydrology: interpreting the hydrogen-isotopic composition of lipid biomarkers from photosynthesizing organisms. Annu Rev Earth Planet Sci 2012;40:221–49.
[30] Wang C, Hren MT, Hoke GD, et al. Soil *n*-alkane δD and glycerol dialkyl glycerol tetraether (GDGT) distributions along an altitudinal transect from southwest China: evaluating organic molecular proxies for paleoclimate and paleoelevation. Org Geochem 2017;107:21–32.
[31] Jia G, Wei K, Chen F, et al. Soil *n*-alkane δD vs. altitude gradients along Mount Gongga, China. Geochim Cosmochim Acta 2008;72:5165–74.
[32] Mügler I, Sachse D, Werner M, et al. Effect of lake evaporation on δD values of lacustrine *n*-alkanes: a comparison of Nam Co (Tibetan Plateau) and Holzmaar (Germany). Org Geochem 2008;39:711–29.
[33] Liu Z, Wen X, Brady EC, et al. Chinese cave records and the East Asia Summer Monsoon. Quat Sci Rev 2014;83:115–28.
[34] Pausata FSR, Battisti DS, Nisancioglu KH, et al. Chinese stalagmite δ^{18}O controlled by changes in the Indian monsoon during a simulated Heinrich event. Nat Geosci 2011;4:474–80.
[35] J. Hoefs. Stable isotope geochemistry: fourth completely revised, updated, and enlarged edition. Berlin: Springer-Verlag, 1996, pp 201.
[36] Collins WD, Bitz CMML. The community climate system model version 3 (CCSM3). J Clim 2006;19:2122–43.
[37] Berger A. Long-term variations of daily insolation and quaternary climatic changes. J Atmos Sci 1978;35:2362–7.
[38] Joos F, Spahni R. Rates of change in natural and anthropogenic radiative forcing over the past 20,000 years. Proc Natl Acad Sci USA 2008;105:1425–30.
[39] McManus JF, Francois R, Gherardi J-M, et al. Collapse and rapid resumption of Atlantic meridional circulation linked to deglacial climate changes. Nature 2004;428:834–7.
[40] Peltier W. Global glacial isostasy and the surface of the ice-age earth: the ICE-5G (VM2) model and GRACE. Annu Rev Earth Planet Sci 2004;32:111–49.
[41] He F. Simulating transient climate evolution of the last deglaciation with CCSM3. Doctor Dissertation. Madison: University of Wisconsin-Madison; 2011.
[42] Liu Z, Carlson AE, He F, et al. Younger Dryas cooling and the Greenland climate response to CO_2. Proc Natl Acad Sci USA 2012;109:11101–4.
[43] He F, Shakun JD, Clark PU, et al. Northern Hemisphere forcing of Southern Hemisphere climate during the last deglaciation. Nature 2013;494:81–5.
[44] Otto-Bliesner BL, Russell JM, Clark PU, et al. Coherent changes of southeastern equatorial and northern African rainfall during the last deglaciation. Science 2014;346:1223–7.
[45] Liu Z, Otto-Bliesner BL, He F, et al. Transient simulation of last deglaciation with a new mechanism for bolling-allerod warming. Science 2009;325:310–4.
[46] Yao T, Masson-Delmotte V, Gao J, et al. A review of climatic controls on δ^{18}O in precipitation over the Tibetan Plateau: observations and simulations. Rev Geophys 2013;51:525–48.
[47] H.G. Liu. Human activities and agriculture resources utilization from Paleolithic to Bronze Age in northwest Yunnan Province. Doctor Dissertation. Lanzhou: Lanzhou University, 2016 (in Chinese).

[48] Wang Q, Yang X, Anderson NJ, et al. Direct versus indirect climate controls on Holocene diatom assemblages in a sub-tropical deep, alpine lake (Lugu Hu, Yunnan, SW China). Quat Res 2016;86:1–12.
[49] Reimer PJ, Bard E, Bayliss A, et al. IntCal13 and Marine13 radiocarbon age calibration curves, 0-50,000 years cal BP. Radiocarbon 2013;55:1869–87.
[50] Blaauw M. Methods and code for 'classical' age-modelling of radiocarbon sequences. Quat Geochronol 2010;5:512–8.
[51] Paillard D, Labeyrie L, Yiou P. Macintosh Program performs time-series analysis. Eos Trans Am Geophys Un 1996;77:39.
[52] Feng X, Zhao C, D'Andrea WJ, et al. Temperature fluctuations during the Common Era in subtropical southwestern China inferred from brGDGTs in a remote alpine lake. Earth Planet Sci Lett 2019;510:26–36.
[53] Zhao B, Zhang Y, Huang X, et al. Comparison of *n*-alkane molecular, carbon and hydrogen isotope compositions of different types of plants in the Dajiuhu peatland, central China. Org Geochem 2018;124:1–11.
[54] De Jonge C, Hopmans EC, Stadnitskaia A, et al. Identification of novel penta- and hexamethylated brached glycerol dialkyl glycerol tetraethers in peat using HPLC–MS2, GC–MS and GC–SMB-MS. Org Geochem 2013;54:78–82.
[55] De Jonge C, Hopmans EC, Zell CI, et al. Occurrence and abundance of 6-methyl branched glycerol dialkyl glycerol tetraethers in soils: implications for palaeoclimate reconstruction. Geochim Cosmochim Acta 2014;141:97–112.
[56] Tian L, Wang M, Zhang X, et al. Synchronous change of temperature and moisture over the past 50 ka in subtropical southwest China as indicated by biomarker records in a crater lake. Quat Sci Rev 2019;212:121–34.
[57] Mohtadi M, Prange M, Oppo DW, et al. North Atlantic forcing of tropical Indian Ocean climate. Nature 2014;509:76–80.
[58] Loomis SE, Russell JM, Verschuren D, et al. The tropical lapse rate steepened during the Last Glacial Maximum. Sci Adv 2017;3:e1600815.
[59] Mark BG, Harrison SP, Spessa A, et al. Tropical snowline changes at the last glacial maximum: a global assessment. Quat Int 2005;138-139:168–201.
[60] Bereiter B, Eggleston S, Schmitt J, et al. Revision of the EPICA Dome C CO_2 record from 800 to 600 kyr before present. Geophys Res Lett 2015;42:542–9.
[61] Petit JR, Jouzel J, Raynaud D, et al. Climate and atmospheric history of the past 420,000 years from the Vostok ice core, Antarctica. Nature 1999;399:429–36.
[62] Members NGRIP. High-resolution record of Northern Hemisphere climate extending into the last interglacial period. Nature 2004;431:147–51.
[63] Friedrich T, Timmermann A, Tigchelaar M, et al. Nonlinear climate sensitivity and its implications for future greenhouse warming. Sci Adv 2016;2: e1501923.
[64] Lu H, Liu W, Yang H, et al. 800-kyr land temperature variations modulated by vegetation changes on Chinese Loess Plateau. Nat Commun 2019;10:1958.
[65] Peterse F, Martínez-García A, Zhou B, et al. Molecular records of continental air temperature and monsoon precipitation variability in East Asia spanning the past 130,000 years. Quat Sci Rev 2014;83:76–82.
[66] Gao Li, Nie J, Clemens S, et al. The importance of solar insolation on the temperature variations for the past 110 kyr on the Chinese Loess Plateau. Palaeogeogr Palaeoclimatol Palaeoecol 2012;317-318:128–33.
[67] Rostek F, Bard E, Beaufort L, et al. Sea surface temperature and productivity records for the past 240 kyr in the Arabian Sea. Deep Sea Res Part II 1997;44:1461–80.
[68] Raza T, Ahmad SM, Steinke S, et al. Glacial to Holocene changes in sea surface temperature and seawater $\delta^{18}O$ in the northern Indian Ocean. Palaeogeogr Palaeoclimatol Palaeoecol 2017;485:697–705.
[69] Schulte S, Müller P. Variations of sea surface temperature and primary productivity during Heinrich and Dansgaard-Oeschger events in the northeastern Arabian Sea. Geo-Mar Lett 2001;21:168–75.
[70] Zhang Y, Zhu K, Huang C, et al. Asian winter monsoon imprint on Holocene SST changes at the northern coast of the South China Sea. Geophys Res Lett 2019;46:13363–70.
[71] Moffa-Sanchez P, Rosenthal Y, Babila TL, et al. Temperature evolution of the Indo-Pacific Warm Pool over the Holocene and the last deglaciation. Paleoceanogr Paleoclimatol Palaeoecol 2019;34:1107–23.
[72] Böll A, Schulz H, Munz P, et al. Contrasting sea surface temperature of summer and winter monsoon variability in the northern Arabian Sea over the last 25 ka. Palaeogeogr Palaeoclimatol Palaeoecol 2015;426:10–21.
[73] Huguet C, Kim JH, Sinninghe Damste JS, et al. Reconstruction of sea surface temperature variations in the Arabian Sea over the last 23 kyr using organic proxies TEX_{86} and $U^{K'}_{37}$. Paleoceanography 2006;21:PA3003.
[74] Berke MA, Johnson TC, Werne JP, et al. Molecular records of climate variability and vegetation response since the Late Pleistocene in the Lake Victoria basin, East Africa. Quat Sci Rev 2012;55:59–74.
[75] Marsicek J, Shuman BN, Bartlein PJ, et al. Reconciling divergent trends and millennial variations in Holocene temperatures. Nature 2018;554:92–6.
[76] Bader J, Jungclaus J, Krivova N, et al. Global temperature mode shed light on the Holocene temperature conundrum. Nat Commun 2020;11:4726.
[77] Leduc G, Schneider R, Kim J-H, et al. Holocene and Eemian sea surface temperature trends as revealed by alkenone and Mg/Ca paleothermometry. Quat Sci Rev 2010;29:989–1004.
[78] Berke MA, Johnson TC, Werne JP, et al. A mid-Holocene thermal maximum at the end of the African Humid Period. Earth Planet Sci Lett 2012;351-352:95–104.
[79] Loomis SE, Russell JM, Lamb HF. Northeast African temperature variability since the Late Pleistocene. Palaeogeogr Palaeoclimatol Palaeoecol 2015;423:80–90.
[80] Chevalier M, Chase BM. Southeast African records reveal a coherent shift from high- to low-latitude forcing mechanisms along the east African margin across last glacial–interglacial transition. Quat Sci Rev 2015;125:117–30.
[81] Tierney JE, Russell JM, Huang Y, et al. Northeast African temperature variability since the Late Pleistocene. Science 2008;322:252–5.
[82] Powers LA, Johnson TC, Werne JP, et al. Large temperature variability in the south African tropics since the Last Glacial Maximum. Geophys Res Lett 2005;32:L08706.
[83] Hou J, Li C-G, Lee S. The temperature record of the Holocene: progress and controversies. Sci Bull 2019;64:565–6.
[84] Rohling EJ, Medina-Elizalde M, Shepherd JG, et al. Sea surface and high-latitude temperature sensitivity to radiative forcing of climate over several glacial cycles. J Climate 2012;25:1635–56.
[85] Castañeda IS, Schouten S, Pätzold J, et al. Hydroclimate variability in the Nile River Basin during the past 28,000 years. Earth Planet Sci Lett 2016;438:47–56.

Cheng Zhao received his Ph.D. degree in Earth and Environmental Sciences from the Department of Earth and Environmental Sciences, Lehigh University (USA) in 2009. After graduation, he worked at the University of Hong Kong and the University of Southampton (UK). Since 2013, he has worked in Nanjing Institute of Geography and Limnology, Chinese Academy of Sciences as a full professor. His research interest includes lake sediments and climate changes, stable and organic geochemistry.

Ji Shen received his bachelor degree from Nanjing University in 1985, and Ph.D. degree from the Department of Geosciences in Nanjing University in 1991. Since then, He has worked in Nanjing Institute of Geography and Limnology, Chinese Academy of Sciences and promoted as a full professor in 1996. In 2020, he joined the School of Geography and Ocean Science in Nanjing University. His research interest focuses on lake sediments and environmental changes.